Focusing of Airborne Synthetic Aperture Radar Data From Highly Nonlinear Flight Tracks

Othmar Frey, *Member, IEEE*, Christophe Magnard, *Student Member, IEEE*, Maurice Rüegg, *Member, IEEE*, and Erich Meier

Abstract—Standard focusing of data from synthetic aperture radar (SAR) assumes a straight recording track of the sensor platform. Small nonlinearities of airborne platform tracks are corrected for during a motion-compensation step while maintaining the assumption of a linear flight path. This paper describes the processing of SAR data acquired from nonlinear tracks, typical of sensors mounted on small aircraft or drones flying at low altitude. Such aircraft do not fly along straight tracks, but the trajectory depends on topography, influences of weather and wind, or the shape of areas of interest such as rivers or traffic routes. Two potential approaches for processing SAR data from such highly nonlinear flight tracks are proposed, namely, a patchwise frequency-domain processing and mosaicking technique and a time-domain back-projection-based technique. Both are evaluated with the help of experimental data featuring tracks with altitude changes, a double bend, a 90° curve, and a linear flight track. In order to assess the quality of the focused data, close-ups of amplitude images are compared, impulse response functions of a point target are analyzed, and the coherence is evaluated. The experimental data were acquired by the German Aerospace Center's E-SAR L-band system.

Index Terms—Corridor mapping, curvilinear synthetic aperture radar, digital elevation model (DEM), extended chirp scaling (ECS), geocoding, georeferencing, integrated focusing and geocoding, mapping, mosaicking, nonlinear flight tracks, synthetic aperture radar (SAR), SAR processing, time-domain back-projection (TDBP).

I. INTRODUCTION

PROCESSING of raw synthetic aperture radar (SAR) data to obtain focused data products is central to virtually all SAR applications and techniques known at present. While being the first and crucial step toward accurate and reliable results of any SAR application, it is also a delicate one, with a strong dependence on the system specifications, flight geometry, and scene properties. For SAR data collected by airborne sensors, the flight path and its incorporation into the processing of the recorded data are of paramount importance. The traditional approach of strip-map SAR begins by assuming an ideal linear

flight path. The SAR data are then reassigned to the linear flight path by one or two so-called motion-compensation steps, whereby small deviations of the sensor from the ideal linear trajectory are compensated.

The extended chirp scaling (ECS) algorithm [1], for instance, implements a two-step motion-compensation approach: 1) A first-order range-invariant motion compensation is performed, and 2) a second-order range-dependent motion compensation is executed before the azimuth compression.

However, SAR systems mounted on small aircraft or even drones may exhibit highly nonlinear—if not arbitrary—flight paths, to the extent that a model of a linear sensor trajectory is no longer feasible. This scenario may occur due to various factors such as rugged topography, atmospheric turbulence, and also the need for more flexibility in mission design. Examples include airborne- or drone-based monitoring of curvilinear areas of interest (corridor mapping), such as rivers and nearby (potential) flooding areas or traffic routes.

In such cases, the model assumption of a single linear trajectory, upon which the standard frequency-domain processing methods are based, is not sufficient, and therefore, more flexible processing approaches must be sought after.

A. Nonlinear Flight Tracks: Previous Work

SAR imaging from nonlinear flight tracks has been an issue of interest for several years. A number of publications that discuss aspects of SAR imaging from nonlinear flight paths have appeared. Soumekh [2] treats the special case of a circular sensor trajectory around the area of interest. In [3] and [4], the idea of using a nonlinear sensor trajectory in the azimuth-elevation plane for tomographic SAR imaging has been proposed. In [5], SAR and other synthetic aperture imaging systems are considered, in which a backscattered wave is measured from positions along an arbitrary flight path. In [6], 3-D tomographic SAR imaging is investigated for several nonlinear trajectory patterns, with the help of simulated data. The focusing performance is compared for various curved flight tracks, including circles, ellipses, spirals, and random sampling. Most of the simulations are carried out for Ka-band SAR systems; for the image formation, a time-domain correlation algorithm is used. Most recently, Xiangle and Ruliang [7] and Su *et al.* [8], [9] studied the performance of 3-D SAR imaging from nonlinear tracks, mainly in the azimuth-elevation plane, with respect to 3-D target reconstruction using parametric and nonparametric estimation techniques. Vigurs and Wood [10] presented a technique exploiting a nonlinear sensor trajectory

to distinguish the Doppler effects of a target's radial velocity from the effect of a cross-range displacement.

The focus of this paper lies on the performance of 2-D SAR imaging from highly nonlinear flight paths. Previous work in this field has been done by Soumekh [11], where the problem of processing SAR data from nonlinear flight tracks is treated in detail and two solutions are proposed. The first solution is processing the data by time-domain back-projection (TDBP). However, the problem is described with the help of a 2-D formulation of the geometry similar to the formulation made in [12], and there is no description of how the changing antenna pointing direction (i.e., the highly varying Doppler centroid) is handled over azimuth. The second solution proposed is an $\omega - k$-based subaperture processing algorithm, which is claimed to yield superior results as compared with the TDBP approach. Unfortunately, neither of these publications provides results obtained using real SAR data acquired from highly nonlinear flight tracks. This paper attempts to fill this gap by presenting experimental results accompanied by the description and comparison of two potential approaches for processing SAR data acquired from highly nonlinear flight tracks.

B. TDBP Processing

Although the possibility of correlating SAR data in the time domain has already been discussed by Barber [13] and later by Courlander and McDomough [14] and Soumekh [12], most of the attention in the SAR processing community has been directed toward more efficient frequency-domain focusing techniques. These algorithms are often designed for processing SAR data of a particular sensor or sensor type. Their general applicability is limited by restrictions imposed upon parameters, such as the maximum chirp bandwidth or the maximum azimuth beam width, and, particularly, the requirement of a regularly shaped (typically linear) sensor trajectory.

More recently, in [15] and [16], fast back-projection techniques have been described. The algorithm presented in [15] makes use of an approximation in the form of a factorization of both the synthetic aperture and the size of the reconstruction grid. The approach in [16] describes a rather similar scheme, where the synthetic aperture is divided into a number of sub-apertures, which are then back-projected to a polar coordinate system with a coarse cross-range resolution. After upsampling of the low-resolution (in azimuth) polar grids, these are coherently added to form the final high-resolution image. With the help of such approximations, the computational complexity can be reduced, albeit at the cost of less accurate phase information. Standard TDBP processing has also been discussed in [12]. However, only the cases of a linear flight track with the usual motion errors and the special case of a circular flight track are discussed.

The authors believe that for many scientific purposes, the amount of time spent on SAR raw data focusing, be it in the frequency domain or *even in the time domain*, is rather small, if not negligible, as compared with the overall time spent on data evaluation and the analysis of derived products. In the particular case of TDBP processing, the data can be split into an arbitrary number of patches that can be processed in parallel with very little interprocess communication. An exception is obviously any true real-time SAR application, given the performance of a realistic current hardware environment. However, for most other cases, looking at the total time spent on data processing and exploitation, the often-cited time factor supporting frequency-domain processing techniques diminishes, particularly if traded for processing quality or if applied to nonstandard SAR data-acquisition scenarios, as will be shown in this paper.

As a side benefit, quicklooks can be generated with increasing resolution without additional processing. Furthermore, the processing can be applied to a subregion of the acquired scene, thus saving time by not requiring the rest of the data to be processed at the same resolution. Potentially, data processing could even begin at acquisition time, with contributions from each echo cumulatively and coherently added as the sensor moves along the azimuth direction; one would not need to wait until the correlation length in azimuth has been reached.

The authors therefore believe that it is well worth exploring the possibilities of TDBP processing, with its inherent ability to generate high-quality results even for SAR data acquired under atypical circumstances.

C. Aim of This Paper

In this paper, two different approaches that have been identified to be potentially suitable for handling highly nonlinear sensor trajectories are discussed:

1) a piecewise track-linearization, processing, and mosaicking approach based on the ECS algorithm (ECS&M);
2) a TDBP processing approach which easily adapts to the changing flight geometry and antenna pointing direction.

The merits and limitations of these two approaches are highlighted by applying them to three airborne SAR data sets acquired from different nonlinear flight tracks. A data set acquired from a quasi-linear track over the same area is used for comparison.

In addition, the focusing performance of the TDBP approach is evaluated quantitatively by examining the impulse response of an in-scene corner reflector. For comparison, a simulated point target having the same position as the corner reflector is evaluated in the same way. During the simulations, the 3-D coordinates and attitude data of the real sensor have been used to ensure comparability between the simulated and the real data.

This paper is organized as follows. Section II discusses the two focusing approaches that were applied to the SAR data from highly nonlinear flight tracks. In Section III, the SAR experiment, as well as the methods used to evaluate the focusing quality of the algorithms, is described. Section IV provides the results in the form of close-ups of amplitude images, impulse response figures for a simulated point target and a trihedral corner reflector, and coherence maps for two image pairs of a small subregion. A discussion of the results follows in Section V, and finally, conclusions are drawn in Section VI.

II. PROCESSING OF NONLINEAR FLIGHT TRACKS

A. Patchwise Frequency-Domain Processing and Mosaicking

Frequency-domain processing algorithms such as the range-Doppler [17], [18], $\omega - k$ [19], or (extended) chirp scaling [1], [20] approaches feature high focusing accuracy while remaining highly efficient. However, they all rely on regular data alignment. Relatively small deviations from a given linear sensor path can be corrected by realigning the data to the linear path by applying motion-compensation algorithms [21]. However, large deviations from a linear track, such as in the case of intentionally nonlinear flight paths, are more difficult to handle.

These limitations may be overcome by approaches where individually focused subpatches of the data set are stepped together (e.g., [22]). To ensure a correct stepping of these single-look complex (SLC) data patches from a strongly non-linear recording path, additional location corrections for the individual patches need to be made, either by image matching or, as presented here, by geocoding.

The algorithm described here is based on airborne SAR raw data. A first patch of the raw data is extracted, i.e., an azimuth segment of a predetermined length is selected and focused using ECS with motion compensation and linearization of the small patch, as described in [21]. The central part in azimuth of the focused patch—containing information from the full synthetic aperture—is subsequently geocoded onto the underlying terrain [23], [24]. The next patch of the raw data is then defined such as to partially overlap in azimuth with the previous patch. The new patch is processed, focused, and geocoded into the output map geometry. This process is repeated until the entire raw data set has been processed. The mosaicking procedure is shown in Fig. 1.

The geocoding step begins with a forward projection into a map geometry, where the corners of the selected patch are geocoded to determine the area of interest. If it is the first patch, an empty geocoded image is created with the dimensions of the area of interest. Otherwise, the previous geocoded image is read and resized to include the new area of interest. An overlap always exists between the newly geocoded patch and the previously mosaicked patch of the mosaic. Overlapping may be as much as 50% of the patch; this is the case for the results presented in Section III. Output samples within overlap zones are produced by weighted averaging of the input samples.

The backward geocoding step, whose aim is to append a patch to the geocoded mosaic, starts from a set of coordinates on the ground and finds the corresponding position within the current SLC patch. This involves selecting a ground position, deriving its terrain height from a digital elevation model (DEM), and calculating a vector between the back-scattering element and the antenna position, using the navigation data and the Doppler centroid frequency from the ECS focusing step. The sensor position and the length of the range vector provide the azimuth and range coordinates within the SLC; the data are extracted at these coordinates and mapped to the mosaic.
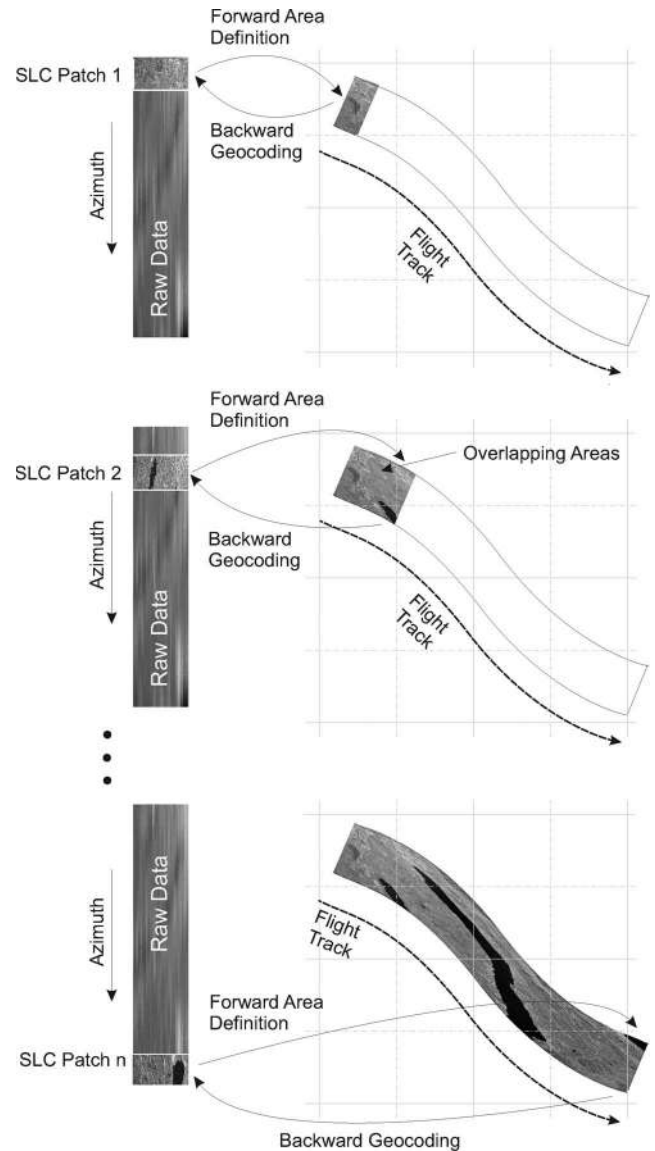

Fig. 1. Schematic illustration of mosaicking through geocoding of the individually focused subpatches of the data set.

Considering that geocoding a focused SAR image, which is described by slant-range and azimuth coordinates, is not a one-to-one operation, resampling of the SAR data is needed (e.g., cubic B-spline [25], [26]). To obtain a smooth geocoded image, an averaging filter can be applied.

Consequently, certain conditions need to be met in order to obtain a precisely mosaicked and geocoded image from a non-linear flight track with the method described earlier. The flight direction must be nearly constant over the length of the synthetic aperture for each patch. If this condition is not met, image blurring will occur. Furthermore, the Doppler centroid frequency may vary by more than half a pulse-repetition frequency (PRF) between two successive patches; this leads to ghost targets or data gaps in the scene, as well as bad focusing of certain parts of the image. In this case, a solution may be to process the image once more with smaller patches and/or smaller steps between the patches. However, the desired azimuth resolution, i.e., the correlation length in azimuth, sets a lower limit on the patch length.

B. TDBP

1) Methodology: Our TDBP implementation has been described in [27] and [28]. Implementation details on aspects such as processing steps, parallelization, hardware used and computational cost are given in Section II-B-2.

In the following, the focus lies mainly on the extension that makes the algorithm suitable for processing SAR data acquired from an arbitrary flight track. The key items of the TDBP approach which enable successful focusing of such SAR data are as follows.

1) By processing the data in the time domain, the exact 3-D configuration of the acquisition pattern and the surface of the illuminated area can be exploited—to the extent that the motion of the aircraft is accurately measured and an accurate digital elevation/surface model is available. In other words, the exact reference function is determined for each point of the reconstruction grid based on the 3-D coordinates of the target points and of the sensor along the synthetic aperture.
2) The Doppler centroid frequency is determined from the sensor's velocity, position, and attitude data and is updated for each radar echo.
3) The varying boundaries of the Doppler bandwidth over azimuth are compared with the Doppler frequency under which the individual target points are "seen." The signal contributions to a certain point on the reconstruction grid are weighted based on the Doppler frequency or omitted if the Doppler frequency exceeds the Doppler boundaries.
4) The scene is divided into a user-defined number of patches that can be processed in parallel in order to overcome the high computational burden of the TDBP approach.

In the following, it is described how the variation of the antenna look direction caused by the nonlinear flight geometry is accounted for during azimuth focusing. For each radar echo j, the Doppler centroid frequency f_{dc_j} is calculated from the navigational data assuming an Earth-centered rotating (ECR) coordinate system, e.g., the WGS84 coordinate system and zero target velocity

$$f_{\mathrm{dc}_j} = \frac{2}{\lambda_c} \cdot \frac{\vec{v}_{S_j} \cdot \vec{p}_j}{|\vec{p}_j|} \tag{1}$$

where λ_c is the wavelength of the carrier signal, $\vec{v}_{S_j}$ is the velocity vector of the sensor corresponding to the jth radar echo, and $\vec{p}_j$ is a vector indicating the antenna pointing direction. $\vec{p}_j$ is calculated from the sensor's positioning and attitude data (roll, pitch, and heading) and is updated for each radar echo. Usually, the velocity vector $\vec{v}_{S_j}$ is directly available from navigational data that accompany the SAR raw data. The pointing vector $\vec{p}_j$ varies as the attitude of the sensor platform changes along the nonlinear flight track. $\vec{p}_j$ is obtained from the aircraft-fixed constant antenna pointing vector $\vec{p}_B$ by the following procedure.

First, $\vec{p}_B$ is left-multiplied by the following azimuth-varying rotation matrices in order to obtain the antenna pointing vector

$\vec{p}_{\mathrm{ned}_j}$ in the topocentric northing–easting–down (NED) coordinate space

$$M_{\theta_{h_j}} = \begin{bmatrix} \cos\theta_{h_j} & -\sin\theta_{h_j} & 0 \\ \sin\theta_{h_j} & \cos\theta_{h_j} & 0 \\ 0 & 0 & 1 \end{bmatrix} \tag{2}$$

$$M_{\theta_{p_j}} = \begin{bmatrix} \cos\theta_{p_j} & 0 & \sin\theta_{p_j} \\ 0 & 1 & 0 \\ -\sin\theta_{p_j} & 0 & \cos\theta_{p_j} \end{bmatrix} \tag{3}$$

$$M_{\theta_{r_j}} = \begin{bmatrix} 1 & 0 & 0 \\ 0 & \cos\theta_{r_j} & -\sin\theta_{r_j} \\ 0 & \sin\theta_{r_j} & \cos\theta_{r_j} \end{bmatrix} \tag{4}$$

$$\vec{p}_{\mathrm{ned}_j} = M_{\theta_{h_j}} M_{\theta_{p_j}} M_{\theta_{r_j}} \vec{p}_B. \tag{5}$$

θ_{h_j} is the *heading*, θ_{p_j} is the *pitch angle*, and θ_{r_j} is the *roll angle*, which, together, define the coordinate transformation between the aircraft's frame of reference and the topocentric NED frame. Note that the rotation angles vary with azimuth. The coordinates are then transformed from the topocentric NED frame to the ECR coordinate system by left-multiplying the rotation matrix M_{T2G_j} to the antenna pointing vector $\vec{p}_{\mathrm{ned}_j}$ in NED coordinates

$$M_{\mathrm{T2G}_j} = \begin{bmatrix} -\sin\Phi_j \cdot \cos\Lambda_j & -\sin\Lambda_j & -\cos\Phi_j \cdot \cos\Lambda_j \\ -\sin\Phi_j \cdot \sin\Lambda_j & \cos\Lambda_j & -\cos\Phi_j \cdot \sin\Lambda_j \\ \cos\Phi_j & 0 & -\sin\Phi_j \end{bmatrix} \tag{6}$$

Φ_j is the latitude, and Λ_j is the longitude. The azimuth-varying antenna pointing vector $\vec{p}_j$, in ECR coordinates, is calculated as

$$\vec{p}_j = M_{\mathrm{T2G}_j} \vec{p}_{\mathrm{ned}_j}. \tag{7}$$

Inserting $\vec{p}_j$ into (1) yields the azimuth-varying reference Doppler centroid frequency f_{dc_j} calculated from geometry, which is later used in order to determine the contributions of the individual radar echoes to a particular target position. Aside from the variation along the flight direction, the Doppler centroid also changes as a function of the elevation angle. This effect is accounted for by calculating the Doppler centroid frequency for three different elevation angles at each sensor position. A polynomial is then determined, which best describes the variation.

Using f_{dc_j}, the azimuth-varying upper and lower limits of the Doppler bandwidth to process are given by $f_{d_{\max j}} = f_{\mathrm{dc}_j} + B/2$ and $f_{d_{\min j}} = f_{\mathrm{dc}_j} - B/2$, where B is the constant absolute Doppler bandwidth.

For each pixel i on the reconstruction grid, the Doppler frequency $f_{d_{ij}}$ is calculated based on the varying geometric constellation given by the target position vector on the ground $\vec{r}_i$, the sensor position $\vec{r}_{S_j}$, and the sensor velocity vector $\vec{v}_{S_j}$

$$f_{d_{ij}} = \frac{2}{\lambda_c} \cdot \frac{\vec{v}_{S_j}(\vec{r}_i - \vec{r}_{S_j})}{|\vec{r}_i - \vec{r}_{S_j}|}. \tag{8}$$

During the coherent summation in the time domain, a weighting function $w(df_{d_{ij}})$ is applied, where $df_{d_{ij}} = f_{d_{ij}} - f_{\mathrm{dc}_j}$. The
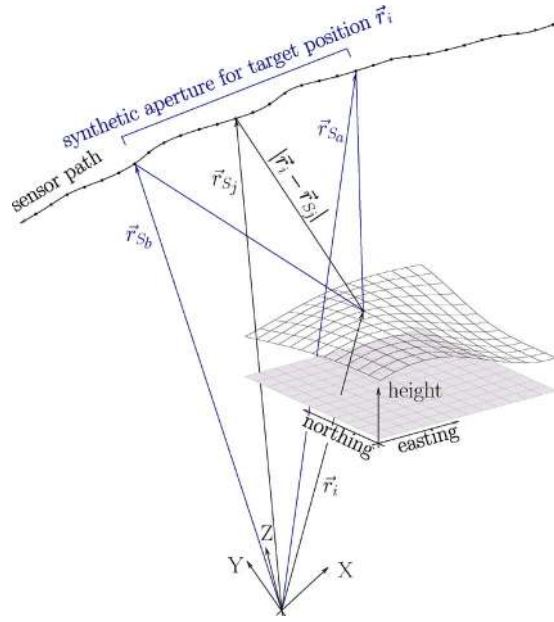
Fig. 2. Schematic view of the acquisition/reconstruction geometry for TDBP processing of SAR data from nonlinear flight tracks.

weighting term w ensures that only signal contributions corresponding to the actual sensor orientation at each azimuth time step are coherently added

$$
w(df_{d_{ij}}) = \begin{cases} \alpha - (1-\alpha)\cos\left(\frac{2\pi df_{d_{ij}}}{B} - \pi\right), & |df_{d_{ij}}| \le \frac{B}{2} \\ 0, & |df_{d_{ij}}| > \frac{B}{2}. \end{cases}
\tag{9}
$$

A value $\alpha = 0.54$ was chosen, which corresponds to a Hamming weighting function. Of course, any other appropriate weighting function can be applied. If the weighting function $w(df_{d_{ij}})$ is incorporated into the TDBP algorithm, the focused signal $s(\vec{r}_i)$ is given as

$$
s(\vec{r}_i) = \sum_{j=a(\vec{r}_i)}^{b(\vec{r}_i)} w(df_{d_{ij}}) \cdot g\left(|\vec{r}_i - \vec{r}_{S_j}|, \vec{r}_{S_j}\right) \cdot |\vec{r}_i - \vec{r}_{S_j}|
$$
$$
\cdot \exp\left(j2k_c|\vec{r}_i - \vec{r}_{S_j}|\right).
\tag{10}
$$

a and b are the indices of the first and last sensor positions, respectively, still contributing to the grid position $\vec{r}_i$. The range-compressed demodulated two-way response is given by $g(.)$ and k_c is the central wavenumber. The acquisition geometry consists of the nonlinear flight track and a reconstruction grid based on a DEM. Fig. 2 shows the general case of a nonlinear flight track and variable terrain. The synthetic aperture and the related geometric elements are shown for the position $\vec{r}_i$ on the reconstruction grid. Note that a and b vary as a function of the grid position $\vec{r}_i$.

Finally, a note is due regarding the calculation of the sampling spacing of the reconstruction grid. Within the TDBP algorithm, the range-compressed data are not focused in the native slant-range/azimuth geometry but are "*back-projected*" to another grid, usually termed the *reconstruction grid* or image space. In order to avoid aliasing, an appropriate sampling

spacing has to be chosen for the reconstruction grid, taking into account the original range and azimuth sampling rates, as well as the shape of the flight track. In particular, attention must be paid to strongly curved tracks, where the direction of illumination varies dramatically during the data acquisition. In such cases the orientation of ground range and azimuth, with respect to the orientation of the reconstruction grid, is continuously changing as the sensor moves along the nonlinear trajectory. Therefore, the output sampling spacing must satisfy the requirements imposed by the varying orientation of ground range and azimuth, such that the focused complex SAR image is never undersampled in either dimension.

2) Implementational Aspects: Our experimental TDBP processor has been realized within a combined Matlab and C++ environment. Tasks such as the preparation of auxiliary data, including navigation data, DEMs, and the subdivision of the data into a number of subpatches to be processed in parallel, are all handled within Matlab. The processor is connected to a coordinate transform engine. Thus, reconstruction grids can be defined for any desired map projection. For the experimental data, each scene has been subdivided into patches of 0.5 km × 1 km in size in the local map projection. The computationally expensive back-projection processing is then performed by an efficient ANSI C++ implementation of the TDBP algorithm. The subsequent collection and mosaicking of the individual patches, as well as data visualization and analysis operations, are again handled by dedicated Matlab scripts. The main processing steps can be summarized as follows.

Processing steps: The processing steps are as follows.

1) Range compression.
2) Preparation of the navigation data.
3) Preparation of the reconstruction grid (may include a DEM) subdivided into a user-defined number of patches in a coordinate system of choice.
4) For each patch, the first and the last contributing echo is determined.
5) The TDBP jobs are sent to the different computing platforms:
   a) Each range-compressed echo is upsampled using a fast Fourier transform (FFT)-based upsampling method [29].
   b) For a sensor position $\vec{r}_{S_j}$ the sensor-to-pixel ranges are calculated for all samples of a patch. Additionally, the Doppler frequency $f_{d_{ij}}$ is evaluated based on (8).
   c) The data values are extracted from the upsampled range echo at the appropriate range distances (rounded to the upsampled sampling spacing), modulated and weighted as described in (10).
   d) The contributions from each echo to a pixel are coherently added until the complete synthetic aperture is reached.
   e) Demodulation.
6) The data patches are assembled and mosaicked.

Parallelization: The subdivision of the scene into several patches, which are then processed individually, permits parallelization of the implementation of the TDBP algorithm. Thus, numerous patches can be processed simultaneously. In
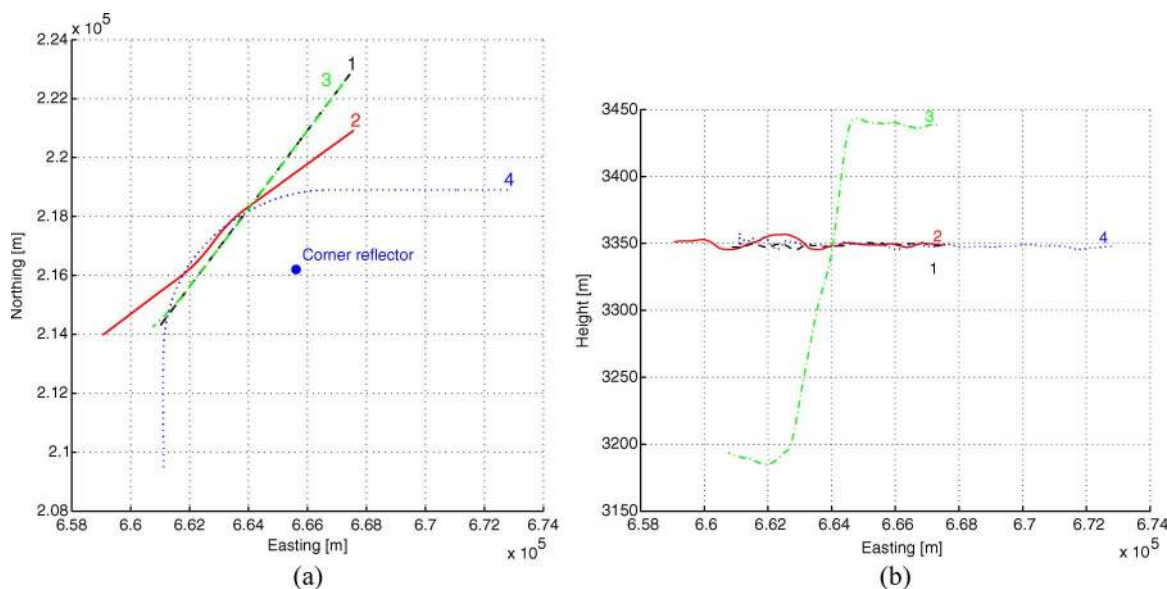
Fig. 3.   Nonlinear flight tracks flown during the experiment, as obtained from the DGPS/IMU system of the E-SAR system. (1, − −) Quasi-linear reference track. (2, —) Double bend. (3, · −) Dive. (4, ··) 90° curve. The position of a corner reflector is shown in (a).

fact, a rather heterogeneous computer cluster (see also the next section) was used for TDBP processing of the experimental data. All machines are accessible via a network and are connected to a centralized array of hard disks for efficient data I/O. This way, interprocess communication is reduced to a minimum. Parallelization of the problem in this way seems to be a flexible and natural solution, particularly because of its *hardware independence*. This type of parallelization is also termed "embarrassing" or "trivial" parallelization, since the parallelization is done at a high level of the algorithm rather than at lower level functions, e.g., the FFT.

Hardware: The experimental data presented in the following section had been focused using a loose network of different computing platforms available at our institute. Among these are a Sun Fire V40z Server, which is equipped with four dual-core AMD Opteron processors Model 880 (2.4 GHz) and a 16-GB RAM running a Linux operating system; several single- and dual-core processor Linux PCs (3.2-GHz clocked Intel Pentium 4) with 1–2-GB RAM; and Mac Pro platforms equipped with two 2.8-GHz Quad-Core Intel Xeon processors and 4-GB RAM. Note that the TDBP processing framework developed here is not hardware specific.

Computational cost: Processing a patch consisting of 10^6 pixels with its center at midrange takes about 10 min on a CPU of a Mac Pro and about 20 min on the Sun Fire or the Linux PCs. Thus, choosing a conservative grid spacing of 0.25 m × 1 m, a scene of 3 km × 4 km can be processed within approximately 1 h using the eight CPUs of a single Mac Pro.

III. DESCRIPTION OF THE EXPERIMENT

A. Experimental Setup

In order to assess the two proposed processing approaches, four tracks were flown by the German Aerospace Center (DLR)'s E-SAR system, namely, a quasi-linear reference track, a track involving a drop in altitude of approximately 250 m

TABLE I
E-SAR L-BAND SYSTEM SPECIFICATIONS

Carrier frequency	1.3 GHz
Chirp bandwidth	94 MHz
Sampling rate	100 MHz
PRF	400 Hz
Ground speed	90 m/s
Azimuth beam width	18°
Elevation beam width	35°
Look direction	left

(*dive*), a double-bend track, and a track with a 90° curve, all shown in Fig. 3.

The system parameters of the L-band sensor used are listed in Table I. The E-SAR system is equipped with a modern computer-controlled CCNS4 navigation system combined with a highly precise differential global positioning system/inertial measurement unit (DGPS/IMU) system of the type AERO-control IId, both by IGI mbH. The absolute 3-D positioning accuracy lies between 0.05- and 0.1-m rms for the available experimental data sets. The short-term relative positioning accuracy is about 0.01-m rms. The accuracy of the attitude angles are given [30] as $\sigma_{\theta_r} = \sigma_{\theta_p} = 0.004°$ rms for the roll and pitch angles and $\sigma_{\theta_h} = 0.01°$ rms for the heading. The velocity is measured with an accuracy of $\sigma_V = 0.005$ m/s, and the bias of the accelerometer $\sigma_b \approx 5 \times 10^{-3}$ m/s². According to Fornaro *et al.* [31], the first derivative of the residual range error, the drift $\sigma_{\dot{\delta}e}$, and the second derivative thereof $\sigma_{\ddot{\delta}e}$ can be expressed as follows:

$$\sigma_{\dot{\delta}e}^2 = \frac{1}{V^2}\sigma_V^2 + (\sin^2\vartheta)\sigma_{\theta_h}^2 \tag{11}$$

$$\sigma_{\ddot{\delta}e}^2 = \frac{1}{V^4}\sigma_b^2 + \left(\frac{g\sin\vartheta}{V^2}\right)^2\sigma_{\theta_r}^2 \tag{12}$$
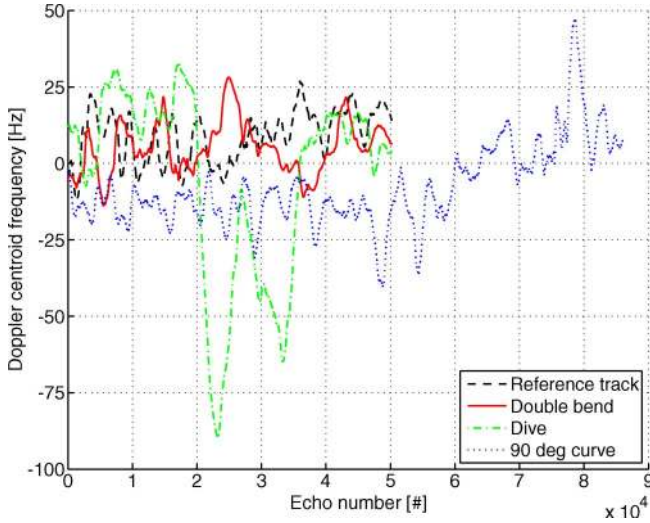
Fig. 4.   Variation of the midelevation Doppler centroid values along the flight track for the four different flight paths, calculated from navigation data.

where V is the platform velocity, $g = 9.81$ m/s^2 is the acceleration due to gravity, and ϑ is the elevation angle, which will be fixed to $45°$. The following values are subsequently obtained for $\sigma_{\dot\delta e}$ and $\sigma_{\ddot\delta e}$:

$$\sigma_{\dot\delta e} = 1.35 \times 10^{-4} \tag{13}$$

$$\sigma_{\ddot\delta e} = 6.2 \times 10^{-7} \text{ m}^{-1}. \tag{14}$$

In addition to the focusing quality, the geometric fidelity of the final image is an important aspect for the user. In order to assess the preservation of dedicated features in the focused image, an airfield has been chosen as a test site. The airfield contains numerous linear elements, such as a runway, fences, and large buildings.

In Fig. 4, the variation of the Doppler centroid values along the flight track is shown for the four different flight paths. The Doppler centroid values are calculated from sensor motion and attitude data, and represent the Doppler centroid values corresponding to the pointing direction of the antenna.

For a quantitative analysis of the impulse response, a trihedral corner reflector, which is visible in all four data sets, was installed on the airfield.

B. Quality Measures for Focused Data

In order to quantify the focusing performance obtained with TDBP processing, the characteristics of the impulse response using the corner reflector, as well as a simulated point target, were measured.

The reader is referred to [32] and [33] for a definition of the numerous quality measures such as the following:

1) three-decibel spatial resolution;
2) peak-to-sidelobe ratio (PSLR);
3) spurious sidelobe ratio;
4) integrated sidelobe ratio (ISLR);
5) ratio of total power to peak height.

IV. RESULTS

First off, some general remarks are needed concerning the evaluation of the results. Qualitative visual comparisons are made of close-up extracts from the airfield area. The processing quality is quantitatively assessed using the measures listed in the previous section. Only the results processed by the TDBP approach are evaluated in detail and compared with the reference track. Detailed analysis of the ECS&M-processed data is not useful here because the SAR images resulting from the frequency-domain/mosaicking approach are not well focused, as shown in Figs. 5 and 6. Two-dimensional frequency plots are presented for all flight tracks processed by TDBP. In addition, coherence maps are given in order to provide area-based measures of processing quality, as opposed to point-target-based measures. Naturally, a useful degree of coherence can only be achieved in cases where the critical baseline criterion is not violated. Further, the look direction in azimuth—or, in other words, the portion of the processed Doppler spectrum—must be identical. At minimum, a considerable overlap is needed. Bearing in mind the flight tracks, which are shown in Fig. 3, it is furthermore clear that the coherence can only be assessed for selected portions and combinations of the four data takes. In the present case, only two combinations of valid data pairs permit the evaluation of the coherence magnitude between the four different flight tracks. Note that the intention of the experiment—and, therefore, the choice of the flight tracks—was not governed by interferometric requirements. Rather, the goal was to make the focusing task as difficult as possible by introducing complicated sensor motions and directional changes during the data acquisition. Nevertheless, the authors believe that the coherence maps provide a useful complementary measure of the focusing performance of the TDBP processor and demonstrate the phase preservation that can be achieved.

The coherence was estimated as follows, as described, for instance, in [34]:

$$\hat\gamma = \frac{\left| \sum_{n=1}^{N} \sum_{m=1}^{M} s_1(n,m) \cdot s_2^*(n,m) \cdot e^{-j\hat\phi(n,m)} \right|}{\sqrt{\sum_{n=1}^{N} \sum_{m=1}^{M} |s_1(n,m)|^2 \cdot \sum_{n=1}^{N} \sum_{m=1}^{M} |s_2(n,m)|^2}} \tag{15}$$

where the interferometric phase $\hat\phi(n,m)$ is estimated beforehand using identical spatial averages. s_1 and s_2 represent the two SAR images. To calculate the spatial averages, $N = M = 5$ is chosen.

A. Image Comparison

In this section, the quality of the images is discussed by comparing close-ups of the same scene extract for all four sensor trajectories and both ECS&M and TDBP algorithms.

1) Quasi-Linear Track: The reference data set acquired from a standard near-linear sensor trajectory is well focused using both processing techniques [see Fig. 5(a) and (b)].

2) Double Bend: In Fig. 5(c), the double-bend data set processed by ECS&M is shown. Considerable defocusing is identified in the southwestern portion of the image. This area
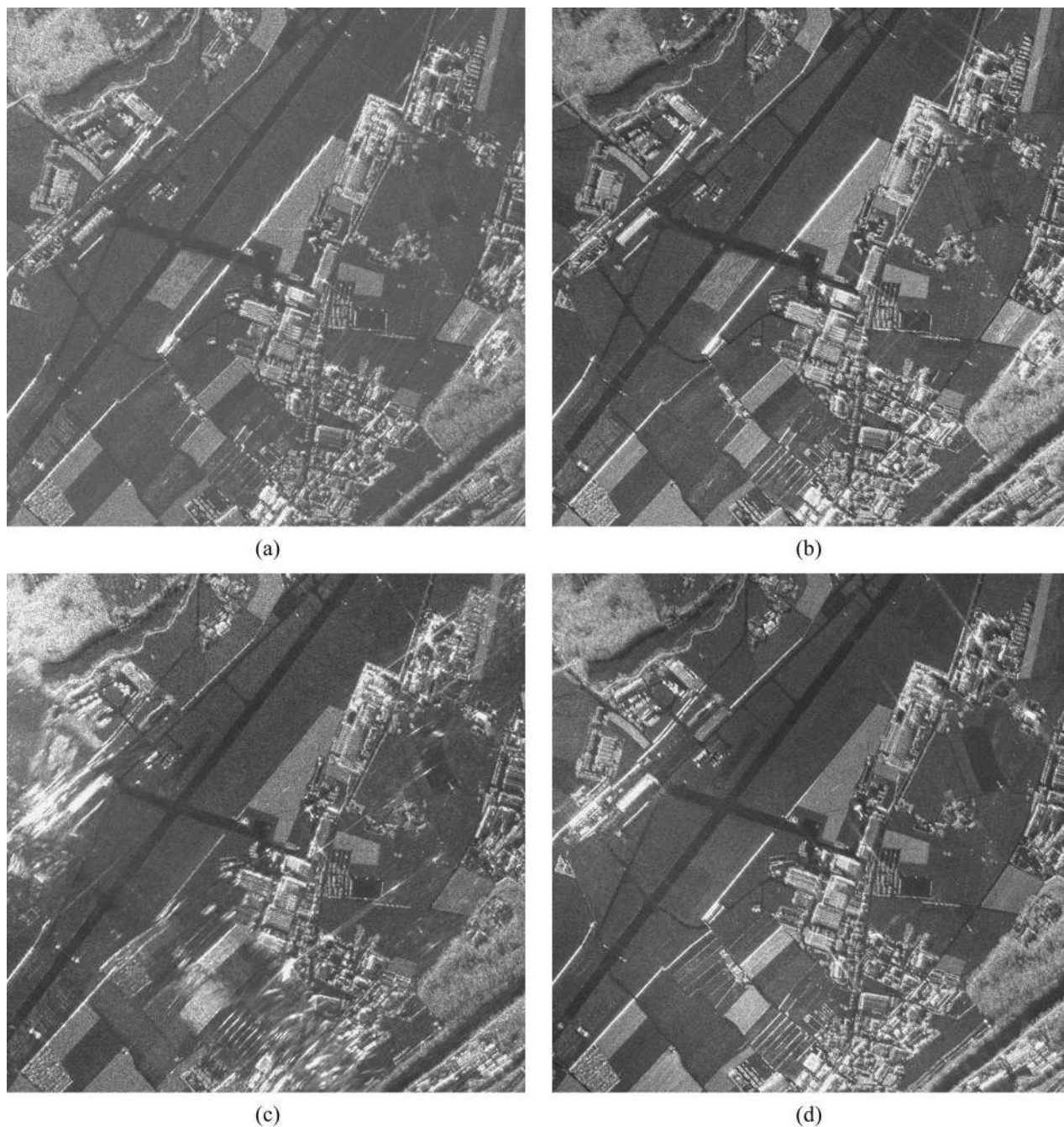
Fig. 5. Close-up views of amplitude images. Sensor: E-SAR L-band HH. (a) ECS and mosaicking: (Quasi-)linear reference track. (b) TDBP: (Quasi-)linear reference track. (c) ECS and mosaicking: Double bend. (d) TDBP: Double bend.

is heavily affected by one of the curves of the double-bend track. For this portion of the flight track, the deviation from the linear subpatches is too large. This, in turn, results from the fact that the number of subpatches is limited by the size of the azimuth beam width. Therefore, a defocused image is obtained. On the other hand, TDBP delivers a well-focused image [see Fig. 5(d)]. Note the slightly positive gradient in brightness from the northeastern to the southwestern corner of the image, best visible along the runway. This effect is due to the azimuth-varying position of the beam center location in the geocoded image, caused by the steeper antenna look angle during the left turn and due to the fact that the elevation antenna gain pattern has intentionally been left uncorrected.

3) Dive: The image resulting from ECS&M [see Fig. 6(a)] appears to be well focused in terms of the geometric resolution; however, a low signal-to-noise ratio is observed. In particular, the image exhibits severe ghost targets [shown by the ellipses in Fig. 6(a)] as a result of the abrupt change in the antenna pointing direction [see also Fig. 4, where a noticeable change in the pointing direction is indicated by the change in the Doppler centroid frequency].

4) 90° Curve: The whole image patch shown in Fig. 6(c), which is approximately situated in the center of the curve, appears blurred. The defocusing is due to the strong curvature of the 90° flight track in combination with the long synthetic aperture of the E-SAR L-band system; for each subpatch, the
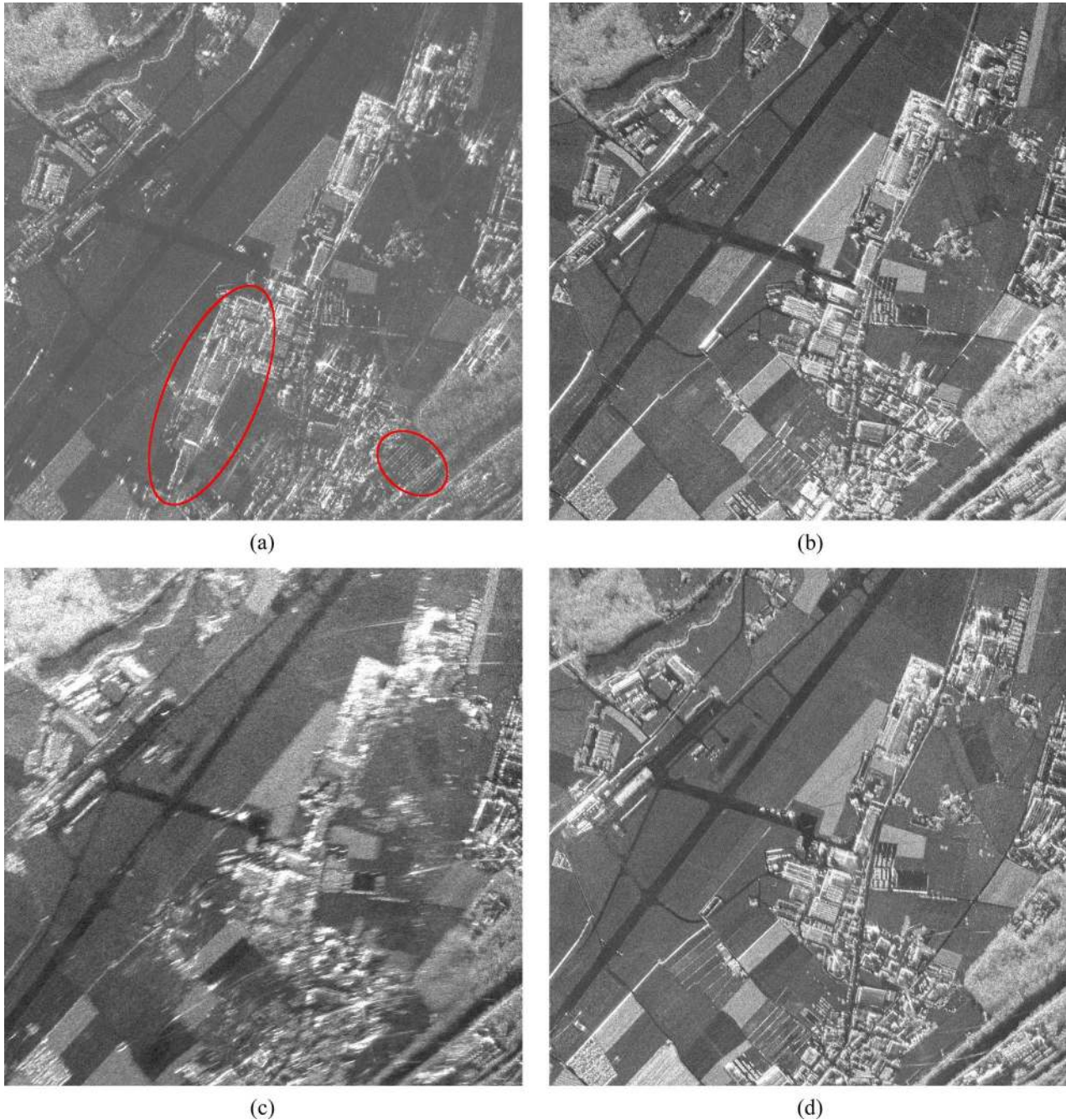
Fig. 6. Close-up views of amplitude images. Sensor: E-SAR L-band HH. (a) ECS and mosaicking: Dive. (b) TDBP: Dive. (c) ECS and mosaicking: 90° curve. (d) TDBP: 90° curve.

deviation of the linearized path from the real sensor trajectory becomes too large toward the ends to still permit an adequate motion compensation within the ECS&M algorithm. In contrast, the TDBP algorithm handles the curved flight geometry very well, and a high focusing quality is obtained [see Fig. 6(d)]. The geometric fidelity appears to be high in all cases, as can be seen by the preservation of linear features, such as the runway and fences.

B. Analysis of the Impulse Response

An analysis of the impulse response function (IRF) was performed for a simulated point target, as well as for a corner reflector visible in the real SAR data set. The simulated point target was assigned the 3-D coordinates of the in-scene corner reflector, which had been deployed on the airfield before the SAR acquisitions. The raw data for the simulated point target was generated using the navigational data of the real flight tracks, providing the identical acquisition geometries required for their comparison.

All impulse response analyses presented here are based on data focused by the proposed TDBP approach. The authors refrain from including the impulse response analyses for the ECS&M approach, since the defocusing and image degradations are immediately clear by visual inspection of Figs. 5 and 6, making further quantitative analysis unnecessary.
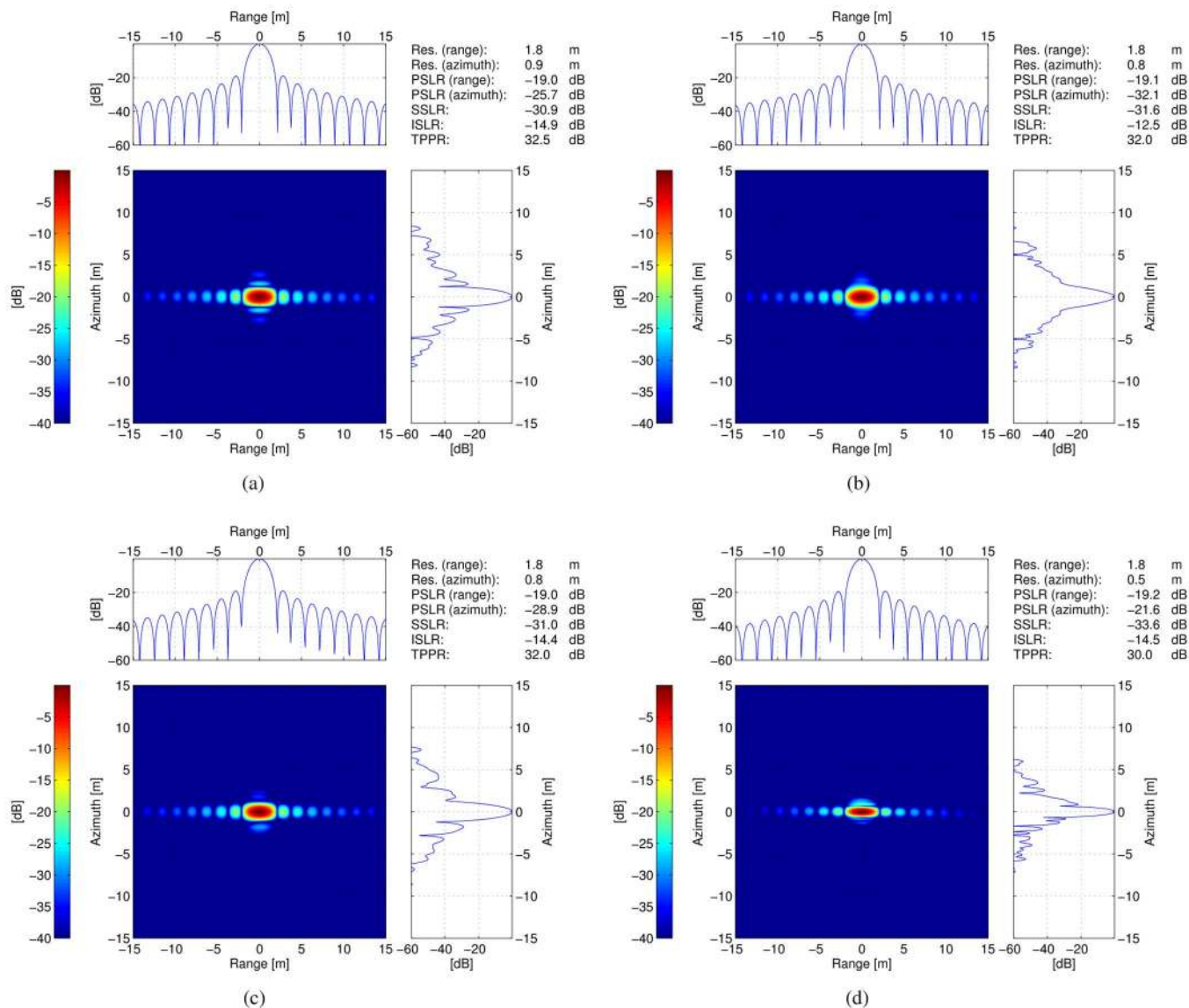
Fig. 7.   Impulse response and quality figures of a simulated point target for all four flight tracks. The location of the simulated point target matches the true location of the trihedral corner reflector that was deployed during the experiment. (a) (Quasi-)linear reference track. (b) Double bend. (c) Dive. (d) 90° curve.

1) Simulated Data: The reason simulated data sets are used to analyze the focusing performance is to demonstrate the focusing quality for a *point target* under ideal conditions.

In Fig. 7, the IRFs for all four simulated data sets are shown, after they have been focused by the TDBP algorithm. The figure annotations list the relevant quality parameters. During range compression, a Kaiser window with coefficient $\beta = 2.12$ was applied, giving a nominal PSLR of ca. -19 dB. This value is approximately equal to the value obtained for the simulated data sets. In the case of the 90° curve, the area surrounding the corner reflector is illuminated in a sliding spotlight manner, and therefore, the azimuth resolution is increased considerably from 0.9 to 0.5 m. Note that the length of the synthetic aperture is altered along the curved flight track. At the beginning and end of the trajectory, where it is approximately linear, the data take resembles strip-map acquisition. Within the curved portion, it approximates a sliding

spotlight acquisition [see also Fig. 3 for the shape of the trajectory].

2) Real Data: Having demonstrated the performance under ideal conditions, the real-world case is now evaluated. The nominal system and processing parameters are identical in both simulated and real cases. Shown in Fig. 8 is the IRF of the TDBP imaging system, evaluated using the in-scene trihedral corner reflector visible in all four SAR images. Compared with the simulated impulse responses, it can be seen that the quality indicators obtained for the corner reflector are inferior for the real data. This is particularly true for the PSLR in range and azimuth, as well as the ISLR. A trihedral corner reflector with triangular reflecting surfaces was used as the reference target. The length of the cathetus of each triangular surface is $a = 1.2$ m, which results in a radar cross section of $\mathrm{RCS} = 4/3 \cdot \mathrm{pi} \cdot a^4/\lambda^2 = 163.42$ m^2 or $\mathrm{RCS_{dB}} = 22.13$ dB $\cdot$ m^2 for the given central wavelength $\lambda = 0.2305$ m of the L-band E-SAR
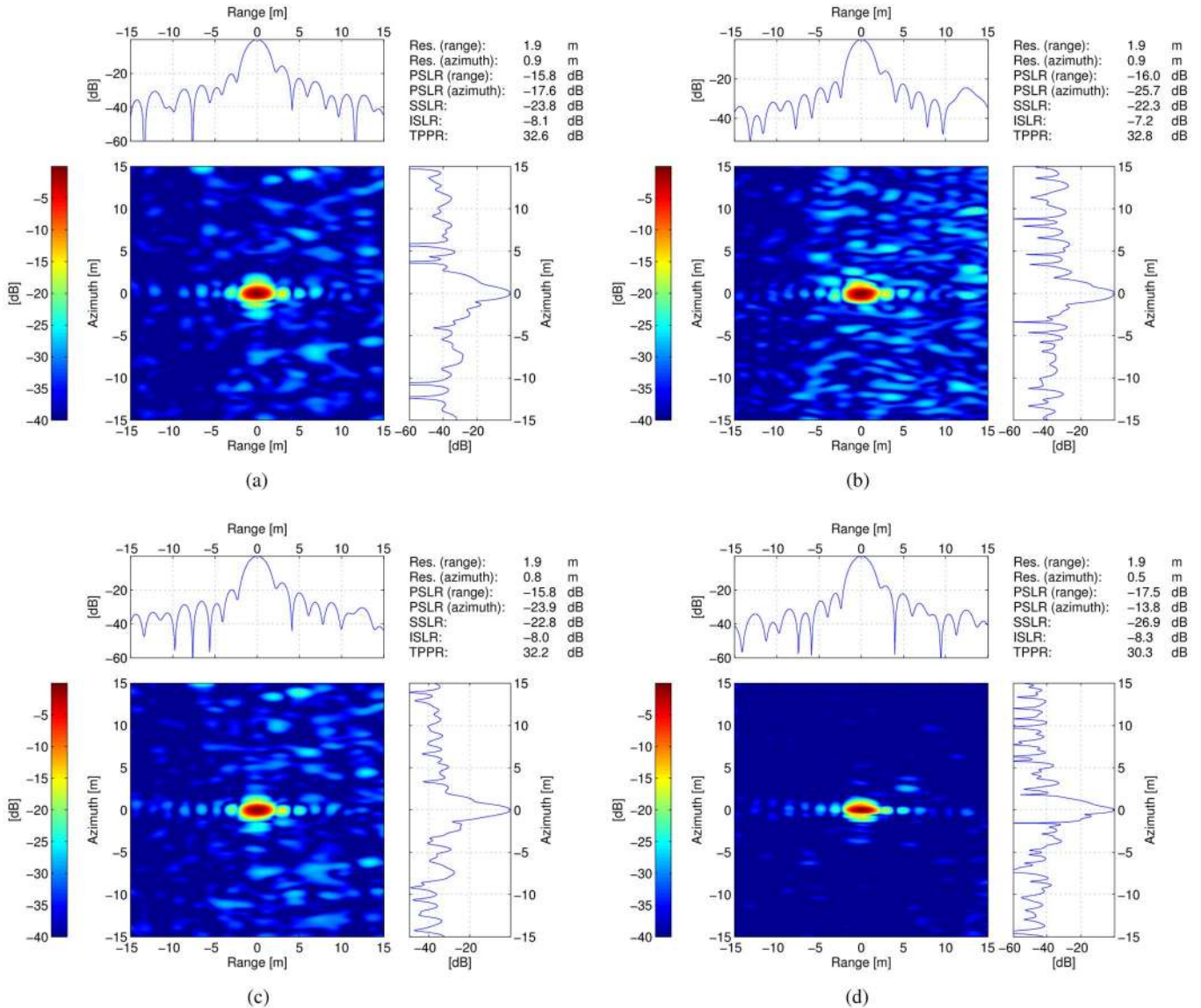
Fig. 8. Impulse response and quality figures of a trihedral corner reflector for all four flight tracks. For the position of the corner reflector, see Fig. 3. (a) (Quasi-)linear reference track. (b) Double bend. (c) Dive. (d) 90° curve.

system. The range resolution of the impulse responses for the real data is approximately 5% lower compared with the simulated case since the effective chirp bandwidth is smaller than the bandwidth used during the simulations. The theoretical value of −19 dB for the range PSLR of the point target is not reached with the real data. The first sidelobe in the far range of the point target is by 1.5–3 dB higher than the theoretical value. Moreover, the azimuth PSLR is affected by anomalous sidelobes, which may have been caused by residual motion errors and interpolation artifacts when preparing the IRF analysis. In contrast with the simulated case, there are many bright targets visible near the corner reflector. These targets have similar or even higher intensity values than the corner reflector. The tarmac on which the reflector was located also exhibits surprisingly high backscatter, affecting the target-to-clutter ratio for the corner reflector. This causes a reduced ISLR compared with the simulated point target.

In terms of azimuth resolution, the impulse responses are equally well focused for both the simulated and real SAR data sets (the resolution has been measured with an accuracy of 10 cm, which corresponds to the sampling spacing of the upsampled impulse response).

However, the most important discovery is that the quality indicators remain *consistent irrespective of the acquisition geometry* for each particular data set, simulated or real. An exception is the azimuth PSLR of the 90°-curved flight, which is considerably lower than in the case of the double-bend or the dive data set. The reason for this difference is the fact that the first azimuth sidelobe is hidden in the main lobe in these cases (see Fig. 8). Apart from that exception, it can be stated that even for the 90° curve flight, the focusing quality is as high as for the quasi-linear reference data set. This demonstrates the ability of the TDBP approach to perform high-quality focusing of all four test cases.
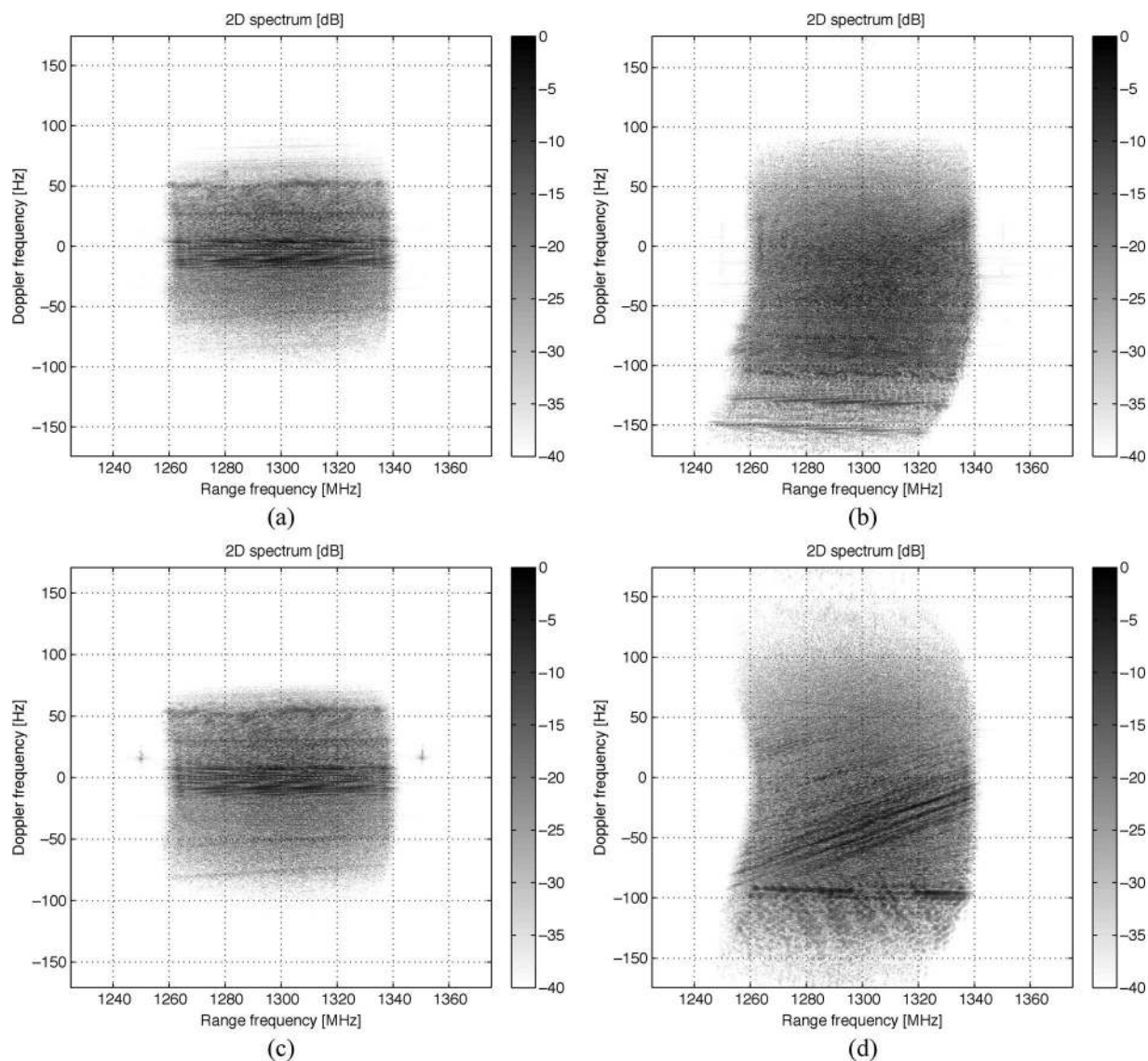
Fig. 9. Two-dimensional power spectra for all four test data sets corresponding to the surrounding area of the in-scene corner reflector. (a) (Quasi-)linear reference track. (b) Double bend. (c) Dive. (d) 90° curve.

In Fig. 9, the 2-D power spectra for the four test cases are shown. There are significant differences, most noticeable in the case of the 90° curve flight and the double-bend track, where an extended Doppler spectrum caused by the curved acquisition geometry can be observed. The spectra were extracted from a part of the scene which includes the corner reflector.

C. Coherence Maps

The corresponding coherence maps for the data pairs *reference track/dive* and *double bend/90° curve* are shown in Fig. 10(a) and (b), respectively. In the case of the *reference track/dive* pair, high coherence values are obtained over a larger area due to the fact that the two flight tracks are more nearly parallel than in the case of the *double bend/90° curve* pair.

Note that the coherence has not been optimized. The Doppler and range spectra have not been reduced to their common spectral band. This is because the coherence is only used as an indicator of phase preservation and focusing quality. Spectral filtering would alter the resolution properties, causing certain regions not to be imaged at all due to the high variability of the relevant Doppler spectrum over azimuth. Neither of these effects is desired; thus, the coherence map is used solely as an indicator of the processing quality.

Indeed, in those areas where the critical baseline criterion is not violated and the look angles coincide, high coherence is obtained. This indicates that the phase is well preserved here, even for the highly nonlinear flight tracks.

D. Complete 90° Curve Flight

In Fig. 11, the amplitude image obtained from TDBP processing of the 90° curve flight is shown, placed on top of a 1 : 25 000-scale map of the area. The data acquisition began in the northeast part of the image, with a heading of 270° and the antenna aimed southward (left-looking antenna). After the aircraft had flown about 5 km to the west, it performed
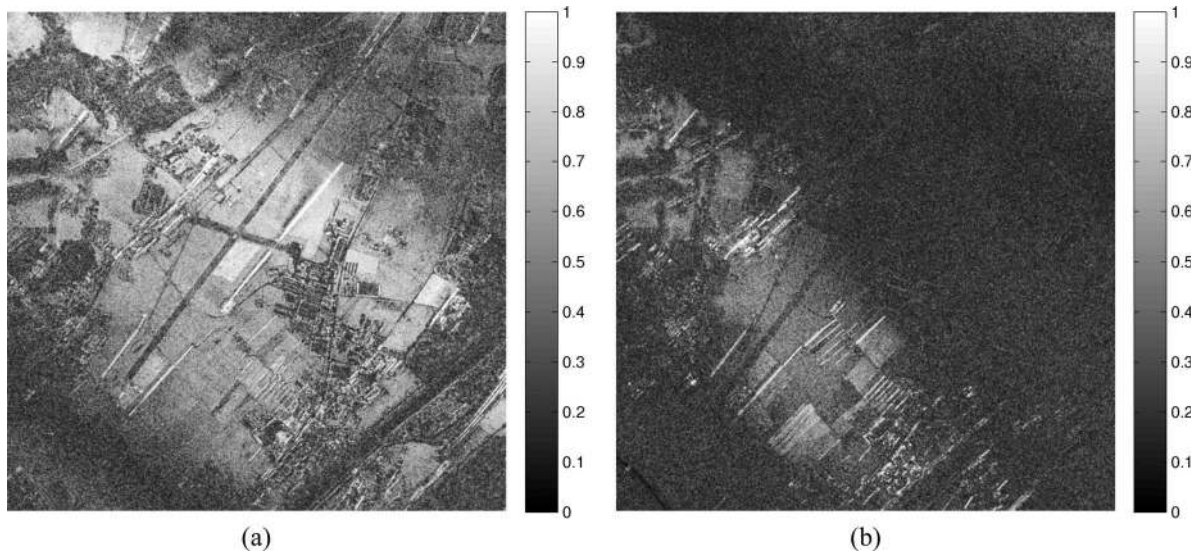
Fig. 10.   Coherence maps for the (a) pairs dive/reference track and (b) double bend/90° curve processed by TDBP. See Fig. 3 for the corresponding sensor trajectories. High coherence values are obtained for the small regions where the flight tracks are well within the critical baseline and where the look direction is similar (note that the coherence is not optimized in the sense that the Doppler and range spectra are reduced to their common spectral band and that the flight tracks of the two data pairs do not run in parallel).
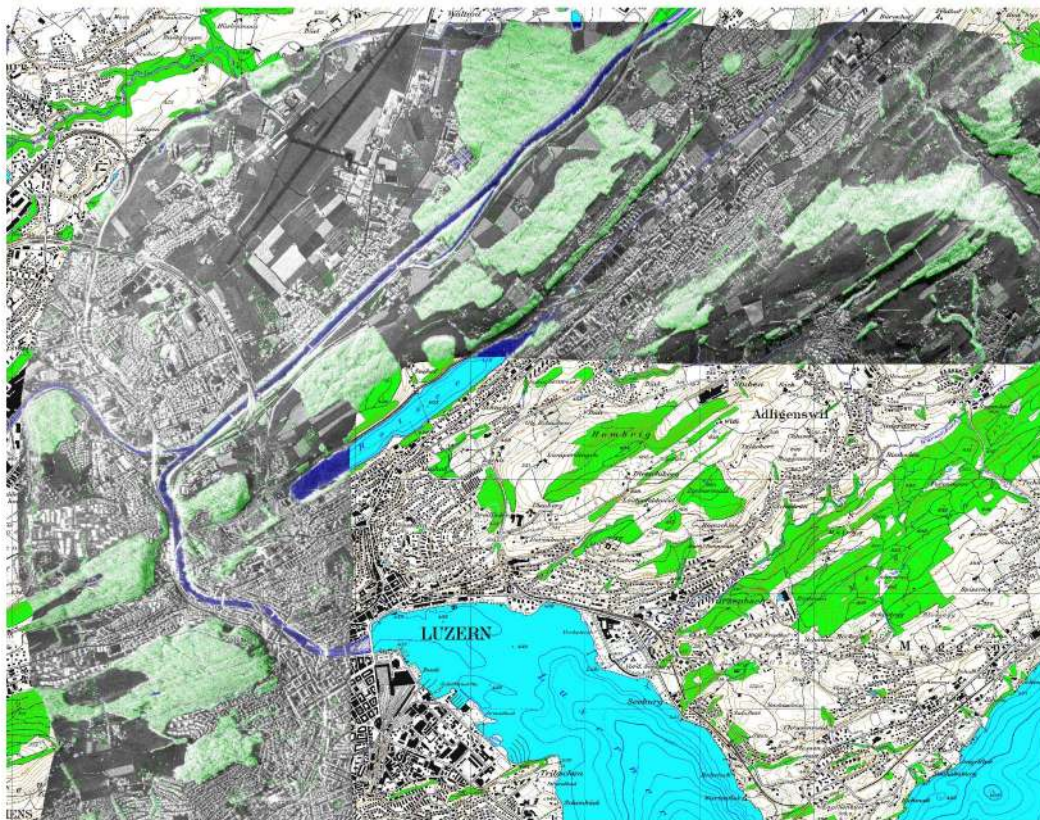

Fig. 11.   Amplitude image of the 90° curve track: E-SAR L-band HH. Processing: TDBP. The data set has been processed directly to map coordinates using a DEM. The SAR amplitude image is shown on top of a 1 : 25 000-scale digital map of the area. Map reproduced by permission of swisstopo (BA081196).

a 90° left turn, resulting in a heading of 180° and an eastward look direction. The data set has been processed onto a DEM given in Swiss map coordinates. The ability of the TDBP approach to process highly nonlinear flight geometries is strikingly demonstrated by the example of this 90°-curved SAR data strip.

V. DISCUSSION

Airborne SAR data acquired from highly nonlinear flight tracks was focused using two processing approaches: 1) a patchwise focusing and mosaicking approach based on the ECS algorithm and 2) a flexible TDBP approach, which utilizes the true 3-D acquisition geometry.

In our experiment, the E-SAR L-band sensor had a moderate azimuth beam width of only $18°$. Nonetheless, the focusing quality of the ECS&M was unsatisfactory, whereas the TDBP approach proposed in this paper provided well-focused results, irrespective of the flight geometry. Its ability to handle difficult 3-D geometry through its inherent consideration of the varying antenna pointing directions during azimuth focusing makes it the superior method. The high focusing performance of the algorithm was demonstrated by point-target analyses and a coherence evaluation of the processed data.

The focusing quality achieved using the ECS&M approach is degraded severely for segments where highly nonlinear sensor motion was present. The major causes are high horizontal (double-bend and $90°$ curve cases) or vertical (dive case) deviations of the linearized subpaths from the original nonlinear flight tracks and, particularly, the considerable variation of the flight direction over the length of the synthetic aperture.

The double bend and the $90°$ curve exhibited maximal deviations of $dn_{max} = 10.6$ m and $dn_{max} = 10.7$ m, respectively. For the dive track, the maximal deviation was $dn_{max} = 9.3$ m, within the length of the synthetic aperture. The quasi-linear reference track, which was well focused by the ECS&M algorithm, had a maximum deviation of $dn_{max} = 1.8$ m. The maximum angle δ_{max} between the velocity vector of the linearized sensor path and the true velocity vectors is $\delta_{max} = 4.9°$ for the double bend, $\delta_{max} = 4.2°$ for the dive, and $\delta_{max} = 5.0°$ for the $90°$ curve. The reference track had a maximum deviation angle of $\delta_{max} = 0.9°$. Thus, in the case of the double bend and the $90°$ curve, the total variation of orientation of the airplane within the length of the synthetic aperture was as high as $8°–10°$. The azimuth antenna beam width limits the number of linearized subpaths along the flight track. However, longer linearized subpath lengths cause larger deviations from the real sensor trajectory and, thus, larger changes in the sensor orientation.

Hence, patchwise frequency-domain processing and mosaicking is limited because of two opposing requirements on the azimuth length of a patch: 1) A higher flight-track nonlinearity would require patches with a shorter azimuth length, and 2) the minimal length of a patch is determined by the azimuth beam width of the antenna. A large azimuth beam width is often preferable in order to ensure a continuous coverage of the region of interest even for large attitude variations along the sensor trajectory.

In an experiment designed to push SAR processing to its limits, it was demonstrated that the proposed TDBP algorithm is a viable and robust processing method when a highly nonlinear sensor trajectory, in combination with a large synthetic aperture, would otherwise cause strong defocusing.

Aside from the higher susceptibility to nonlinear sensor motion, another limitation of the ECS&M approach is that the phase information is not retained in the final mosaicked image. The phase information is preserved when using the TDBP approach, even if the data are directly obtained in the map projection of choice.

A further advantage of the TDBP approach is that it allows any subregion of interest to be processed without the need to process the entire data set.

VI. Conclusion

The TDBP algorithm proposed in this paper is well adapted for producing high-quality images for airborne SAR data from highly nonlinear flight tracks. The high processing quality and geometric fidelity of this method are demonstrated by comparing the results for a region common with all four data sets. A high focusing quality is achieved regardless of the acquisition geometry. The back-projection algorithm generates complex-valued georeferenced SAR images.

In Section I, corridor mapping was mentioned as a potential application, i.e., mapping of curvilinear features such as rivers or traffic routes. The TDBP-based approach provides the means for such mapping tasks—flexible and parallelized processing of dedicated subareas of interest within a SAR data set acquired from virtually arbitrarily shaped flight tracks, combined with direct mapping functionality in any desired coordinate frame and map projection.

References

[1] A. Moreira, J. Mittermayer, and R. Scheiber, "Extended chirp scaling algorithm for air- and spaceborne SAR data processing in stripmap and ScanSAR imaging modes," *IEEE Trans. Geosci. Remote Sens.*, vol. 34, no. 5, pp. 1123–1136, Sep. 1996.

[2] M. Soumekh, "Reconnaissance with slant plane circular SAR imaging," *IEEE Trans. Image Process.*, vol. 5, no. 8, pp. 1252–1265, Aug. 1996.

[3] K. Knaell, "Three-dimensional SAR from curvilinear apertures," in *Proc. SPIE*, Orlando, FL, Jun. 1994, vol. 2230, pp. 120–134.

[4] J. Li, Z. Bi, Z. Liu, and K. Knaell, "Use of curvilinear SAR for three-dimensional target feature extraction," *Proc. Inst. Elect. Eng.—Radar, Sonar Navig.*, vol. 144, no. 5, pp. 275–283, Oct. 1997.

[5] C. J. Nolan and M. Cheney, "Synthetic aperture inversion for arbitrary flight paths and nonflat topography," *IEEE Trans. Image Process.*, vol. 12, no. 9, pp. 1035–1043, Sep. 2003.

[6] S. R. Axelsson, "Beam characteristics of three-dimensional SAR in curved or random paths," *IEEE Trans. Geosci. Remote Sens.*, vol. 42, no. 10, pp. 2324–2334, Oct. 2004.

[7] L. Xiangle and Y. Ruliang, "Study of composite mode curvilinear SAR," in *Proc. Int. Conf. Radar, CIE*, 2006, pp. 1–4.

[8] Z. Su, Y. Peng, and X. Wang, "Evaluation of the aperture in the curvilinear SAR," in *Proc. Int. Conf. Radar, CIE*, 2006, pp. 1–4.

[9] Z. Su, Y. Peng, and X. Wang, "Feature-independent aperture evaluator for the curvilinear SAR," *IEEE Geosci. Remote Sens. Lett.*, vol. 4, no. 2, pp. 191–195, Apr. 2007.

[10] G. Vigurs, M. Wood, and M. Jarrett, "Non-linear synthetic aperture radar techniques," in *Proc. EURAD*, Oct. 2005, pp. 13–16.

[11] M. Soumekh, "Time domain non-linear SAR processing," Dept. Elect. Eng., State Univ. New York, New York, 2006. Tech. Rep.

[12] M. Soumekh, *Synthetic Aperture Radar Signal Processing: With MATLAB Algorithms*. Hoboken, NJ: Wiley, 1999.

[13] B. C. Barber, "Theory of digital imaging from orbital synthetic-aperture radar," *Int. J. Remote Sens.*, vol. 6, no. 7, pp. 1009–1057, 1985.

[14] J. C. Curlander and R. N. McDonough, *Synthetic Aperture Radar—Systems and Signal Processing*. Hoboken, NJ: Wiley, 1991.

[15] L. M. H. Ulander, H. Hellsten, and G. Stenström, "Synthetic-aperture radar processing using fast factorized back-projection," *IEEE Trans. Aerosp. Electron. Syst.*, vol. 39, no. 3, pp. 760–776, Jul. 2003.

[16] A. F. Yegulalp, "Fast backprojection algorithm for synthetic aperture radar," in *Proc. Rec. IEEE Radar Conf.*, 1999, pp. 60–65.

[17] I. G. Cumming and J. R. Bennett, "Digital processing of SEASAT SAR data," in *Proc. Rec. IEEE Int. Conf. Acoust., Speech Signal*, Washington, DC, Apr. 1979, pp. 710–718.

[18] M. Y. Jin and C. Wu, "A SAR correlation algorithm which accommodates large range migration," *IEEE Trans. Geosci. Remote Sens.*, vol. GRS-22, no. 6, pp. 592–597, Jun. 1984.

[19] C. Cafforio, C. Prati, and F. Rocca, "SAR data focusing using seismic migration techniques," *IEEE Trans. Aerosp. Electron. Syst.*, vol. 27, no. 2, pp. 194–207, Mar. 1991.

[20] R. K. Raney, H. Runge, R. Bamler, I. G. Cumming, and F. H. Wong, "Precision SAR processing using chirp scaling," *IEEE Trans. Geosci. Remote Sens.*, vol. 32, no. 4, pp. 786–799, Jul. 1994.

[21] A. Moreira and Y. Huang, "Airborne SAR processing of highly squinted data using a chirp scaling approach with integrated motion compensation," *IEEE Trans. Geosci. Remote Sens.*, vol. 32, no. 5, pp. 1029–1040, Sep. 1994.

[22] M. Soumekh, "Reconnaissance with slant plane circular SAR imaging," *IEEE Trans. Image Process.*, vol. 5, no. 8, pp. 1252–1265, Aug. 1996.

[23] E. Meier, U. Frei, and D. Nüesch, *SAR Geocoding: Data and Systems*. Karlsruhe, Germany: Wichmann, 1993, ch. Precise Terrain Corrected Geocoded Images, pp. 173–186.

[24] A. Schubert, "Stereo-assisted interferometric SAR, Chap. 3.4 geocoding," Ph.D. dissertation, Remote Sens. Lab., Univ. Zurich, Zurich, Switzerland, 2004.

[25] M. Unser, A. Aldroubi, and M. Eden, "B-spline signal processing: Part I—Theory," *IEEE Trans. Signal Process.*, vol. 41, no. 2, pp. 821–832, Feb. 1993.

[26] M. Unser, A. Aldroubi, and M. Eden, "B-spline signal processing: Part II—Efficient design and applications," *IEEE Trans. Signal Process.*, vol. 41, no. 2, pp. 834–848, Feb. 1993.

[27] O. Frey, E. Meier, and D. Nüesch, "Processing SAR data of rugged terrain by time-domain back-projection," in *Proc. SPIE*, Bruges, Belgium, Sep. 2005, vol. 5980, pp. 1–9.

[28] O. Frey, E. Meier, and D. Nüesch, "An integrated focusing and calibration procedure for airborne SAR data," in *Proc. EUSAR*, Dresden, Germany, May 2006, pp. 1–4.

[29] D. Fraser, "Interpolation by the FFT revisited—An experimental investigation," *IEEE Trans. Acoust., Speech, Signal Process.*, vol. 37, no. 5, pp. 665–675, May 1989.

[30] *AEROcontrol IId Product Description,* 2006. [Online]. Available: http://www.igi-systems.com/downloads/specifications/specifications_aero control.pdf

[31] G. Fornaro, G. Franceschetti, and S. Perna, "Motion compensation errors: Effects on the accuracy of airborne SAR images," *IEEE Trans. Aerosp. Electron. Syst.*, vol. 41, no. 4, pp. 1338–1352, Oct. 2005.

[32] ASAR-Cal/Val-Team, *Quality Measurements Definition for ASAR Level 1 Products*, Mar. 2002, Frascati, Italy: ESA. Tech. Rep. Iss. 1.

[33] B. Rosich and P. Meadows, "Absolute calibration of ASAR level 1 products generated with PF-ASAR," ESA, Frascati, Italy, Oct. 2004. Tech. Rep. Iss. 1 rev. 5.

[34] A. Monti Guarnieri and C. Prati, "SAR interferometry: A "Quick and Dirty" coherence estimator for data browsing," *IEEE Trans. Geosci. Remote Sens.*, vol. 35, no. 3, pp. 660–669, May 1997.

Christophe Magnard (S'07) received the M.Sc. degree in microengineering from the Swiss Federal Institute of Technology, Lausanne, Switzerland in 2005.

He has been with the Remote Sensing Laboratories, University of Zurich, Zurich, Switzerland, since 2006, as a Research Assistant. His research interests include multibaseline synthetic aperture radar (SAR) interferometry with millimeter-wave radar and SAR focusing algorithms.

Maurice Rüegg (S'00–M'07) received the M.Sc. degree in electrical engineering from the Swiss Federal Institute of Technology, Zurich, Switzerland, in 2003 and the Ph.D. degree in microwave remote sensing from the Remote Sensing Laboratories, University of Zurich, Zurich, in 2007.

Upon completion of his dissertation, his broader computer science interests led him to private industry. He is currently a Software Engineer with the foreign exchange and money markets business of UBS Investment Bank, Zurich. His research interests included detection techniques for ground moving targets in synthetic aperture radar (SAR), SAR focusing algorithms, data simulations, and millimeter-wave radar.

Othmar Frey (S'04–M'08) received the M.Sc. degree in geomatic engineering (awarded the Swiss Federal Institute of Technology (ETH) medal for an outstanding master thesis) from the ETH Zurich, Zurich, Switzerland, in 2002.

Since 2002, he has been with the Remote Sensing Laboratories, University of Zurich, Zurich, as a Research Associate, where he has worked on a geometric error budget analysis for TerraSAR-X data products and on atmospheric effects in synthetic aperture radar (SAR) data until 2003/2004 and where he is currently working in the field of SAR signal processing. His current research interests include SAR focusing algorithms, in general, and SAR tomography and other advanced SAR imaging modes, in particular. He has developed and implemented a SAR signal-processing software that allows for end-to-end data processing of advanced imaging modes, such as airborne multibaseline SAR and SAR data acquisitions from nonlinear flight tracks.

Mr. Frey has contributed to invited sessions on SAR tomography at the EUSAR 2008 conference and at the International Geoscience and Remote Sensing Symposium'08, where he has also served as a session cochair. He is a Reviewer for the IEEE TRANSACTIONS ON GEOSCIENCE AND REMOTE SENSING and the IEEE GEOSCIENCE AND REMOTE SENSING LETTERS.

Erich Meier received the M.Sc. degree in geography and the Ph.D. (Hons.) degree in remote sensing from the University of Zurich, Zurich, Switzerland, in 1982 and 1989, respectively.

Since 1979, he has been with the University of Zurich, first as a Research Assistant with the Remote Sensing Section until 1982; then, he was with the Geographic Information System Laboratory, Department of Geography, from 1982 to 1983, and then, since 1983, he has been with the Remote Sensing Laboratories (RSL), first as a Research Scientist, until 2006, and where he is currently a Research Section Head involved in teaching and in research on digital image processing, software development for computer graphics, and radiometric and geometric calibration of synthetic aperture radar (SAR) and optical imagery. Moreover, since 2000, he has been the Head of the SARLab, a research group within RSL whose research interests are the development of new focusing algorithms for SAR data from UHF to millimeter-wave; interferometry; polarimetry; MTI algorithms; and calibration and validation activities for spaceborne and airborne systems. He is responsible for the research strategies and the organization of the team. He is a Consultant on behalf of several national and international organizations and private companies.